Lithogeochemical and sulfide trace element systematics across the Permian–Triassic boundary, Perth Basin, Western Australia: Constraints on the shallow marine environment during the End-Permian Mass Extinction

E. Lounejeva[a]*, J. A. Steadman[a], R. R. Large[a], K. Grice[b], P. Olin[a], and I. Belousov[a]

[a] CODES, Centre for Ore Deposit and Earth Sciences, University of Tasmania, Private Bag 79, Hobart, Tasmania, Australia; [b] Western Australian Organic and Isotope Geochemistry Centre, School of Earth and Planetary Science, Curtin University, Perth, Western Australia, Australia

* contact e-mail: elena.lounejeva@utas.edu.au

Elena Lounejeva 0000-0002-2462-8623
Jeffrey Steadman 0000-0003-4679-3643
Ross Large 0000-0003-0012-0101
Kliti Grice 0000-0003-2136-3508
Paul Olin 0009-0003-8630-7029
Ivan Belousov 0000-0002-9224-6408

Received 7 December 2022; accepted 29 March 2023
Editorial handling: Anita Andrew

SUPPLEMENTAL DATA

Australian Journal of Earth Sciences (2023), *70*(5), https://doi.org/10.1080/08120099.2023.2200476

Copies of Supplementary Papers may be obtained from the Geological Society of Australia's website (www.gsa.org.au), the Australian Journal of Earth Sciences website (www.ajes.com.au) or from the National Library of Australia's Pandora archive (https://pandora.nla.gov.au/tep/150555).

Supplemental data

Lounejeva et al. (2023). Supplemental data
Australian Journal of Earth Sciences, 70(5), https://doi.org/10.1080/08120099.2023.2200476

Pyrite Geochemical data (Excel workbook)

Table. List of samples and data used in this study.

SAMPLEID	SPI/INI	Relative depth elevation	Period	Method	Laboratory	Reference
RB2_3791.7	SPI	14.85	Triassic	LA-ICPMS and ME-MS61	1	4
RB2_3792.9	SPI	13.65	Triassic	LA-ICPMS	2	
RB2_3795.7	SPI	10.85	Triassic	LA-ICPMS and ME-MS61	1	4
RB2_3797.3	SPI	9.25	Triassic	LA-ICPMS	2	
RB2_3797.8	SPI	8.75	Triassic	LA-ICPMS and ME-MS61	1	4
RB2_3798.3	SPI	8.25	Triassic	LA-ICPMS and ME-MS61	1	4
RB2_3799.2	SPI	7.35	Triassic	LA-ICPMS and ME-MS61	1	4
RB2_3799.93	SPI	6.62	Triassic	LA-ICPMS and ME-MS61	1	4
RB2_3800.4	SPI	6.15	Triassic	LA-ICPMS and ME-MS61	1	4
RB2_3800.6	SPI	5.95	Triassic	LA-ICPMS and ME-MS61	1	4
RB2_3801.12	SPI	5.43	Triassic	LA-ICPMS and ME-MS61	1	4
RB2_3801.7	SPI	4.85	Triassic	LA-ICPMS and ME-MS61	1	4
RB2_3802.15	SPI	4.40	Triassic	LA-ICPMS and ME-MS61	1	4
RB2_3803.2	SPI	3.35	Triassic	LA-ICPMS and ME-MS61	1	4
?PTB between 3803.76 and 3804.14						
RB2_3803.8		2.75	EPMEI	LA-ICPMS and ME-MS61	1	4
3804.14/3814.5 *P. microcorpus* zone top in RB2 no sample			EPMEI			5
RB2_3804.6	INI	1.95	EPMEI	LA-ICPMS and ME-MS61	1	4
RB2_3805.4	INI	1.15	EPMEI	LA-ICPMS and ME-MS61	1	4
RB2_3806.15	INI	0.40	EPMEI	LA-ICPMS and ME-MS61	1	4
RB2_3806.51	INI	0.04	EPMEI	LA-ICPMS and ME-MS61	1	4
3806.55 level cero in RB2, $\delta^{13}C$						
RB2_3806.55	INI	–	EPMEI	LA-ICPMS and ME-MS61	1	4
RB2_3807.1	INI	–0.55	EPMEI	LA-ICPMS and ME-MS61	1	4
RB2_3807.35	INI	–0.80	EPMEI	LA-ICPMS and ME-MS61	1	4
RB2_3808.13	INI	–1.58	EPMEI	LA-ICPMS and ME-MS61	1	4
RB2_3808.9	INI	–2.35	Permian	LA-ICPMS	2	
RB2_3809.62	INI	–3.07	Permian	LA-ICPMS	2	
RB2_3809.73	INI	–3.18	Permian	LA-ICPMS and ME-MS61	1	4
RB2_3810.4	INI	–3.85	Permian	LA-ICPMS	2	
RB2_3811	INI	–4.45	Permian	LA-ICPMS	2	
RB2_3811.8	INI	–5.25	Permian	LA-ICPMS	2	
RB2_3812.2	INI	–5.65	Permian	LA-ICPMS	2	
RB2_3812.7	INI	–6.15	Permian	LA-ICPMS	2	6
RB2_3813.6	INI	–7.05	Permian	LA-ICPMS and ME-MS61	1	4
RB2_3815.5	INI	–8.95	Permian	LA-ICPMS	2	
RB2_3815.95	INI	–9.40	Permian	LA-ICPMS	2	
RB2_3816.9	INI	–10.35	Permian	LA-ICPMS	2	
RB2_3818.76	INI	–12.21	Permian	LA-ICPMS	2	
RB2_3821.3	INI	–14.75	Permian	LA-ICPMS	2	
RB2_3823.8	INI	–17.25	Permian	LA-ICPMS	2	
RB2_3825.6	INI	–19.05	Permian	LA-ICPMS	2	
RB2_3827.4	INI	–20.85	Permian	LA-ICPMS	2	
RB2_3830.6	INI	–24.05	Permian	LA-ICPMS	2	
RB2_3831.2	INI	–24.65	Permian	LA-ICPMS	2	

SAMPLEID	SPI/INI	Relative depth elevation	Period	Method	Laboratory	Reference
RB2_3832.1	INI	–25.55	Permian	LA-ICPMS	2	
RB2_3834.3	INI	–27.75	Permian	LA-ICPMS	2	
RB2_3835.3	INI	–28.75	Permian	LA-ICPMS and ME-MS61	1	4
HO3-1968.30	SPI	12.65	Triassic	LA-ICPMS	2	
HO3-1968.56	SPI	12.39	Triassic	4 acids	3	7
HO3-1969.06	SPI	11.89	Triassic	LA-ICPMS	2	
HO3-1969.47	SPI	11.48	Triassic	LA-ICPMS	2	
HO3-1970.00	SPI	10.95	Triassic	LA-ICPMS	2	
HO3-1970.91	SPI	10.04	Triassic	4 acids	3	7
HO3-1971.81	SPI	9.14	Triassic	4 acids	3	7
HO3-1973.05	SPI	7.90	Triassic	LA-ICPMS	2	
HO3-1973.31	SPI	7.64	Triassic	4 acids	3	7
HO3-1974.21	SPI	6.74	Triassic	4 acids	3	7
HO3-1974.41	SPI	6.54	Triassic	4 acids	3	7
HO3-1975.56	SPI	5.39	Triassic	4 acids	3	7
HO3-1975.71	SPI	5.24	Triassic	4 acids	3	7
HO3-1976.00	SPI	4.95	Triassic	LA-ICPMS	2	
HO3-1977.21	SPI	3.74	Triassic	4 acids	3	7
HO3-1978.16	SPI	2.79	Triassic	4 acids	3	7
HO3-1978.50	SPI	2.45	Triassic	LA-ICPMS	2	
HO3-1979.00	SPI	1.95	Triassic	LA-ICPMS	2	
HO3-1979.16	SPI	1.79	Triassic	4 acids	3	7
HO3-1979.50	SPI	1.45	Triassic	LA-ICPMS	2	
HO3-1979.51	SPI	1.44	Triassic	4 acids	3	7
HO3-1979.91	SPI	1.04	Triassic	4 acids	3	7
HO3-1980.00	SPI	0.95	Triassic	LA-ICPMS	2	
HO3-1980.03	SPI	0.92	Triassic	LA-ICPMS	2	
HO3-1980.26	SPI	0.69	Triassic	4 acids	3	7
HO3-1980.40	SPI	0.55	Triassic	LA-ICPMS	2	
HO3-1980.56	SPI	0.39	Triassic	4 acids	3	7
HO3-1980.7	SPI	0.25	Triassic	4 acids	3	7
HO3-1980.85 PTB						8
HO3-1980.86	SPI	0.10	EPMEI	4 acids	3	7
HO3-1980.865	SPI	0.09	EPMEI	4 acids	3	7
HO3-1980.875	SPI	0.08	EPMEI	4 acids	3	7
HO3-1980.885	SPI	0.07	EPMEI	4 acids	3	7
HO3-1980.895	SPI	0.06	EPMEI	4 acids	3	7
HO3-1980.905	SPI	0.05	EPMEI	4 acids	3	7
HO3-1980.915	SPI	0.04	EPMEI	4 acids	3	7
HO3-1980.925	SPI	0.03	EPMEI	4 acids	3	7
HO3-1980.93 ?SPI/INI						
HO3-1980.935		0.02	EPMEI	4 acids	3	7
HO3-1980.945		0.01	EPMEI	4 acids	3	7
HO3-1980.95	INI					
HO3-1980.955	INI	–0.00	EPMEI	4 acids	3	7
HO3-1980.965	INI	–0.01	EPMEI	4 acids	3	7
HO3-1980.975	INI	–0.02	EPMEI	4 acids	3	7
HO3-1980.985	INI	–0.03	EPMEI	4 acids	3	7
HO3-1980.995	INI	–0.04	EPMEI	4 acids	3	7

SAMPLEID	SPI/INI	Relative depth elevation	Period	Method	Laboratory	Reference
HO3-1981.00 The last Permian						8
HO3-1981.005	INI	–0.05	Permian	4 acids	3	7
HO3-1981.01	INI	–0.06	Permian	4 acids	3	7
HO3-1981.15	INI	–0.20	Permian	4 acids	3	7
HO3-1981.45	INI	–0.50	Permian	LA-ICPMS	2	
HO3-1981.56	INI	–0.61	Permian	4 acids	3	7
HO3-1981.86	INI	–0.91	Permian	4 acids	3	7
HO3-1982.30	INI	–1.35	Permian	LA-ICPMS	2	
HO3-1983.00	INI	–2.05				
HO3-1983.200	INI	–2.25	Permian	LA-ICPMS	2	
HO3-1983.50	INI	–2.55	Permian	LA-ICPMS	2	
HO3-1983.67	INI	–2.72	Permian	LA-ICPMS	2	
HO3-1984.50	INI	–3.55	Permian	LA-ICPMS	2	
HO3-1985.30	INI	–4.35	Permian	LA-ICPMS	2	
HO3-1985.72	INI	–4.77	Permian	LA-ICPMS	2	
HO3-1985.76	INI	–4.81	Permian	4 acids	3	7
HO3-1985.80	INI	–4.85	Permian	LA-ICPMS	2	
HO3-1986.14	INI	–5.19	Permian	LA-ICPMS	2	
HO3-1986.61	INI	–5.66	Permian	4 acids	3	7
HO3-1986.75	INI	–5.80	Permian	LA-ICPMS	2	
HO3-1987.03	INI	–6.08	Permian	LA-ICPMS	2	
HO3-1987.06	INI	–6.11	Permian	4 acids	3	7
HO3-1987.20	INI	–6.25	Permian	LA-ICPMS	2	
HO3-1987.50	INI	–6.55	Permian	LA-ICPMS	2	
HO3-1987.84	INI	–6.89	Permian	LA-ICPMS	2	
HO3-1988.01	INI	–7.06	Permian	4 acids	3	7
HO3-1988.07	INI	–7.12	Permian	LA-ICPMS	2	
HO3-1989.50	INI	–8.55	Permian	LA-ICPMS	2	
HO3-1990.21	INI	–9.26	Permian	4 acids	3	7
HO3-1992.26	INI	–11.31	Permian	4 acids	3	7
HO3-2009.7 no sample	INI	–28.75				
Hov-1-19				EA/IRMS, IRMS, CVAFS		9

1, CODES and ALS this work

2, CODES Analytical Laboratories

3, Curtin University Laboratories

4, δ^{34}S, TOC and δ^{13}C from Lounejeva *et al.* (2021)

5, Purcell (2010)

6, Large *et al.* (2014)

7, B, δ^{34}S, TOC, TOS and REE - this work, other- Georgiev *et al.* (2020)

8, Thomas *et al.* (2004)

9, Sial *et al.* (2020)

Figure TESPY Downhole patterns

The downhole patterns for trace elements in pyrite (ppm py) from Redback 2 (RB2) and Hove 3 (HO3) boreholes. paired by similar behaviour. Each dot corresponds to geometric mean for framboidal and disseminated pyrite.

- Co-Ni, Ni-As, Co-As

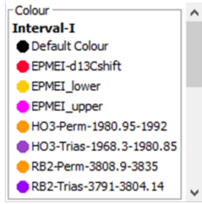

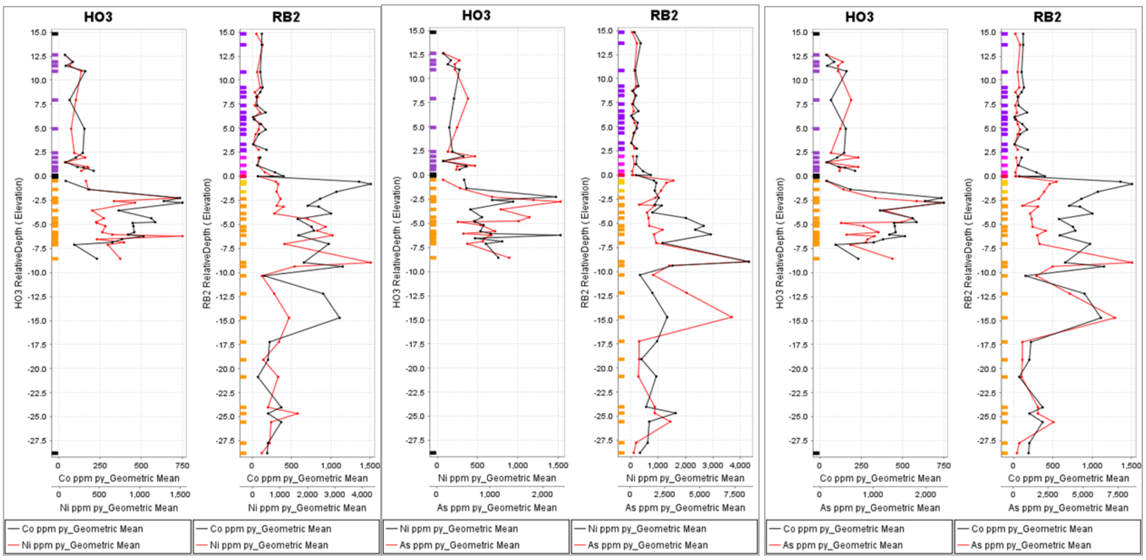

- Mn-Cu, Se-Pb, Zn-Cd

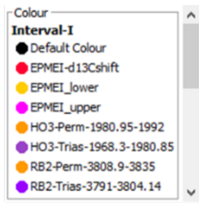

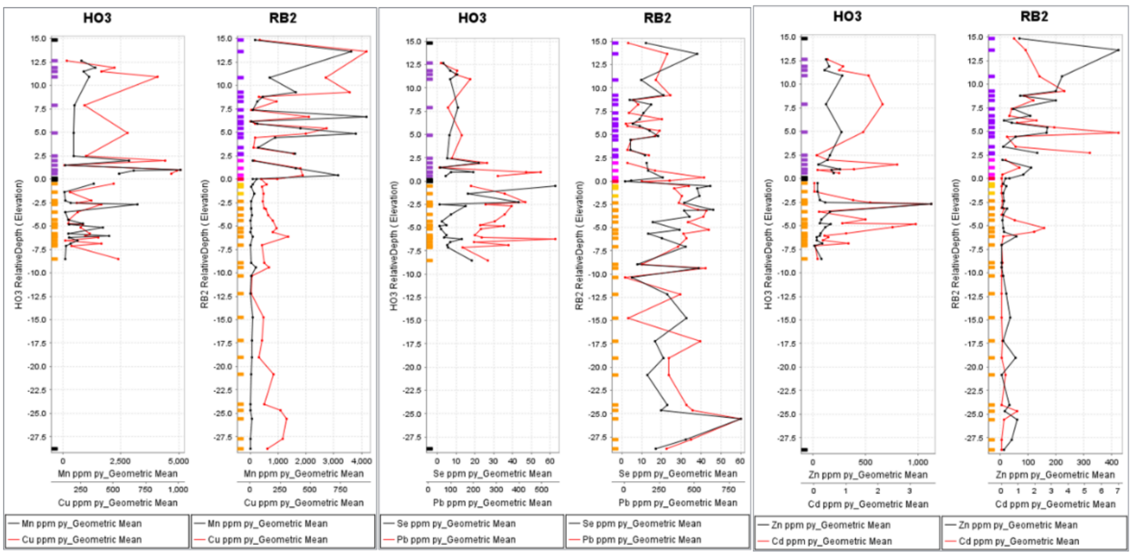

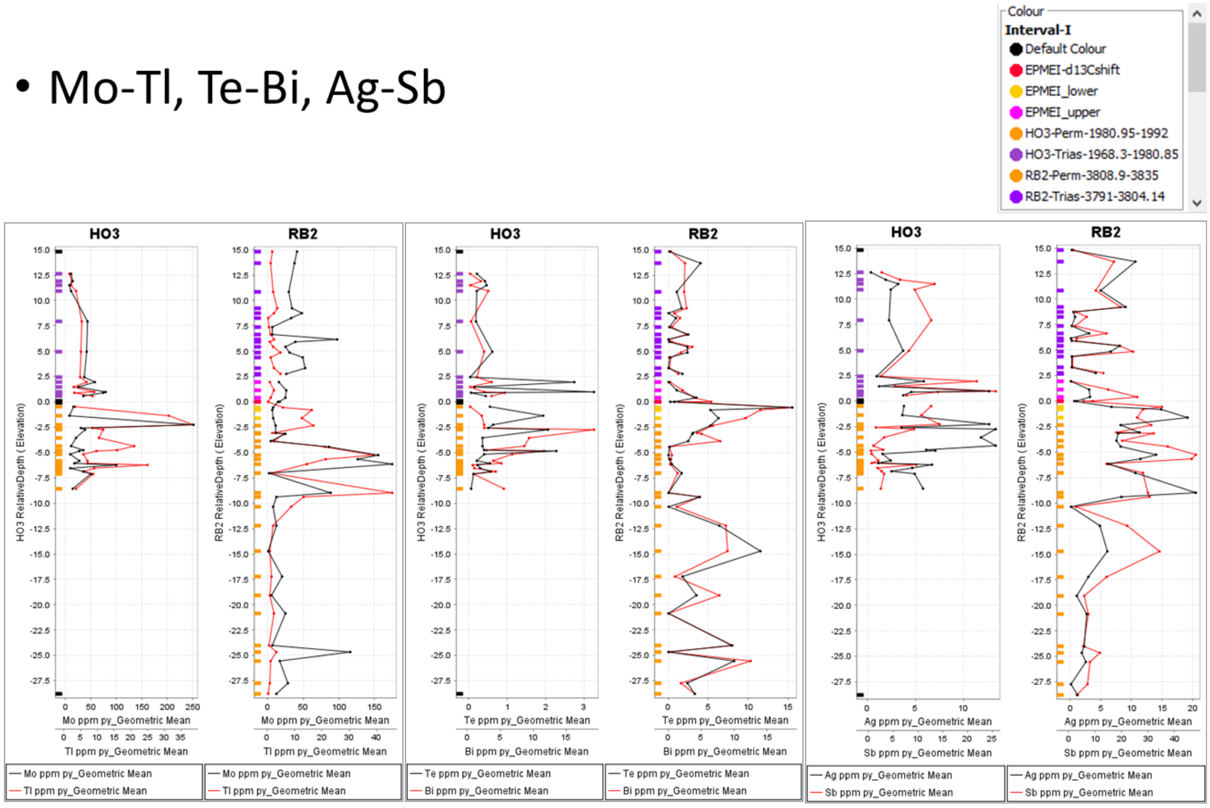

Figure TESPY Scatter plot as an alternative presentation of the main change in trace elements composition of pyrite composition from the Hovea Member sediments

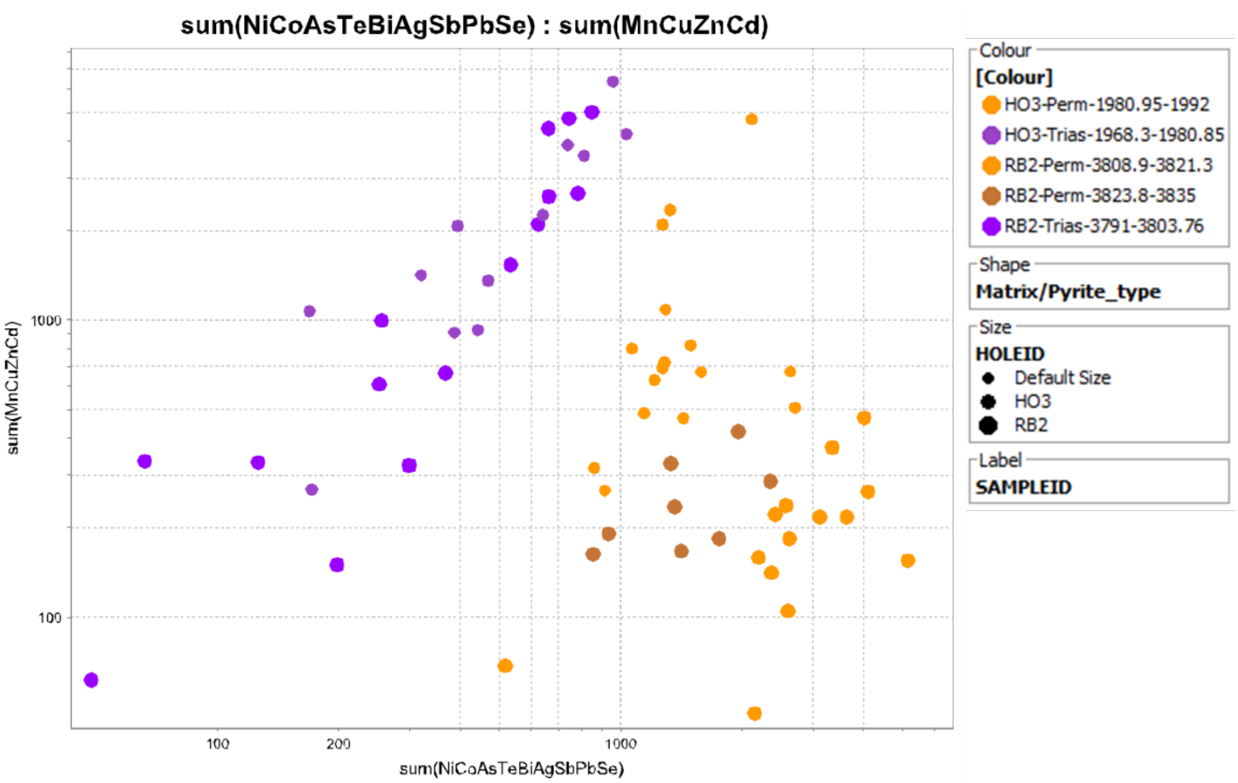

LA-ICPMS analysis specifications.

The trace element contents of pyrite have been analysed across multiple sessions by laser ablation-inductively coupled-mass spectrometry (LA-ICPMS) at CODES Analytical laboratory, University of Tasmania. The instrumentation involved a New Wave UP-213ss Nd-YAG Laser and a RESOlution 193 nm excimer laser, coupled to an Agilent 7700x ICP-MS. We used the laser beam size varying between 10 and 51 microns depending on the size of the pyrite crystals and kept laser fluence between 2.5 and 3.5 J/cm^2 and the repetition rate of 5 Hz. Each analysis included a 30 sec of gas background run (laser off) to properly assess detection limits, followed by a 40–60 sec signal acquisition in time-resolved mode. The primary calibration standards included the in-house reference materials STDGL2b2 (Danyushevsky *et al.,* 2011) and STDGL-3 (Belousov *et al.,* 2014) for quantification of siderophile and chalcophile elements, and the USGS reference material GSD-1G (Jochum *et al.,* 2014), for quantification of lithophile elements. A natural pyrite standard PPP-1 (Gilbert *et al.,* 2014) was used to quantify sulphur. Reference materials were analysed every hour during analytical sessions to correct instrumental drift. For every individual sample of 2 cm shale fragment, 12–15 LA-ICPMS spot analyses were performed on pyrite and five on the surrounding silicate matrix. The analytical method quantifies pyrite and matrix using the above reference materials compositions to get the raw results. The raw results have been reduced using the inhouse-developed method elucidated by Stepanov and collaborators (Stepanov *et al.,* 2020), which is based on the Excel spreadsheets and the Basic scripts templates for mass balance and Fe–S linear regression. In addition, matrix-pyrite deconvolution become possible using the LADR (Laser Ablation Data Reduction) software from Norris Scientific (https://norsci.com/?p=ladr). The ioGAS software from IMDEX (https://iogas.imdexlimited.com) has been used for basic statistics (Supplementary data 3.xlsx) and presentation of the data.

LA-ICPMS data statistics

Dealing with the below detection limits values

Analysis of the results estimated below detection limits and suggests that (1) during the same analytical session, detection limits for elements with a longer washout time (mostly from the V–VI groups of elements, i.e. As, Sb, Bi, Se and Te) may vary up to two orders of magnitude, and (2) Au, Pt, Se, Cd, and Te are of the lowest concentration (≤1 ppm) in the Hovea Member sedimentary pyrites and yet represent a challenge for the LA-ICPMS method [Se (21% <DL), Cd (27%<DL) and Te (33%<DL)]. Most of the results for gold and platinum are not reported as only a few values yielded ≥0.01 ppm with a high grade of uncertainty in the middle of the EPMEI. We assessed the average detection limit for each spot size and the minimal significant value for each element and substituted text “<DL value” by half of the minimal detection limit.

	Detection limit (ppm)					
Spot size (microns)	19	29	51			DL29um/2
55Mn	47.888	5.962	7.598			2.981
59Co	4.581	0.671	0.789			0.3355
60Ni	3.239	1.495	0.725			0.7475
65Cu	19.382	3.086	3.283			1.543
66Zn	20.985	2.965	3.244			1.4825
75As	130.825	21.413	20.813			10.7065
77Se	108.807	31.529	21.447			15.7645
95Mo	0.991	0.112	0.151			0.056
107Ag	6.192	0.413	0.77			0.2065
111Cd	3.082	0.297	0.479			0.1485
121Sb	6.047	0.578	0.801			0.289
125Te	7.476	1.234	1.273			0.617
205Tl	0.85	0.133	0.114			0.0665
208Pb	2.018	0.348	0.301			0.174
209Bi	0.566	0.058	0.077			0.029
Element	**Half-DL**	**# off substitutions**	1023			
Te	0.017	342	33%			
Cd	0.011	279	27%			
Se	0.718	216	21%			
Sb	0.04	66	6%			
Ag	0.0165	62	6%			
Zn	0.0725	16	2%			
Tl	0.008	14	1%			
As	86.46	4	0.4%			
Pb	1.723					
Mo	0.1505					
Cu	0.123					
Bi	0.0025					
As	86.46					

Screening

Statistics were performed on the reduced data set after <DL substitution and filtering out high outliers. The reduced data set includes the data where Cu or Pb are <0.8%, and nickel-normalised ratios are within the limits 0.01<Cu/Ni<2, 0.01<Zn/Ni<10, an 0.1<As/Ni<10, suggested for sedimentary pyrite (Gregory *et al.,* 2015). The only data with As/Ni<0.1 correspond to the pyrite–marcasite intergrowth, as Ni content is very low <100 ppm.

Correlations

The strongest correlation Ni–Co is obvious from the scatter plots below also exposes high contents of Ni and Co in the Permian compared to the Triassic pyrites.

Ni vs. Co

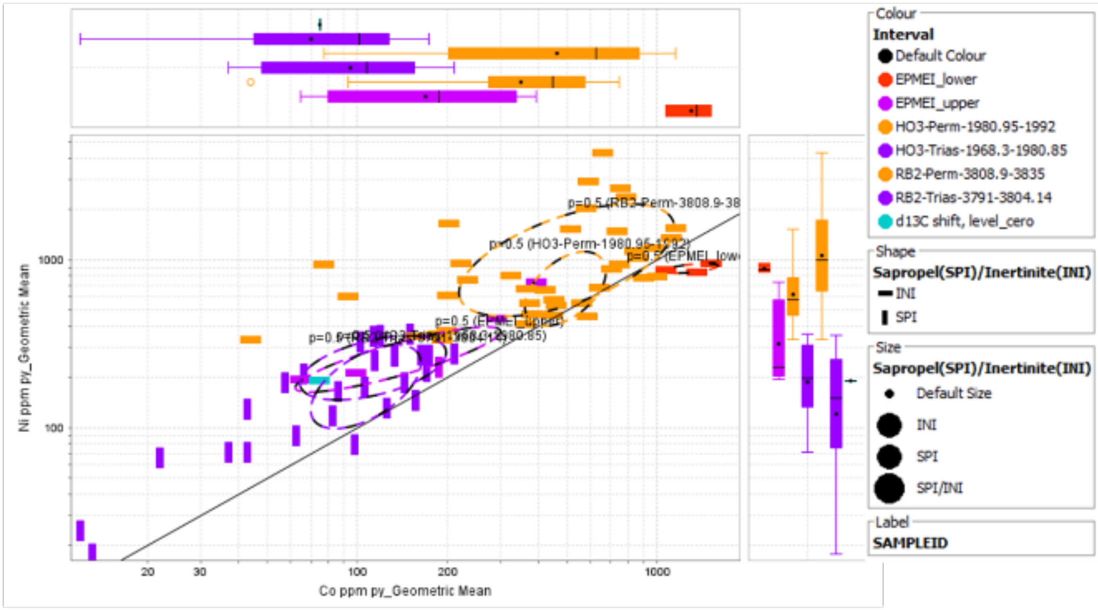

- Spearman correlation factor: Triassic 0.82, Permian 0.39
- Note a break between the two periods (Ni ~300 vs. Co~280 ppm)

The second strong correlation is between Pb and Bi but traceable only in Triassic sediments.

Pb vs. Bi

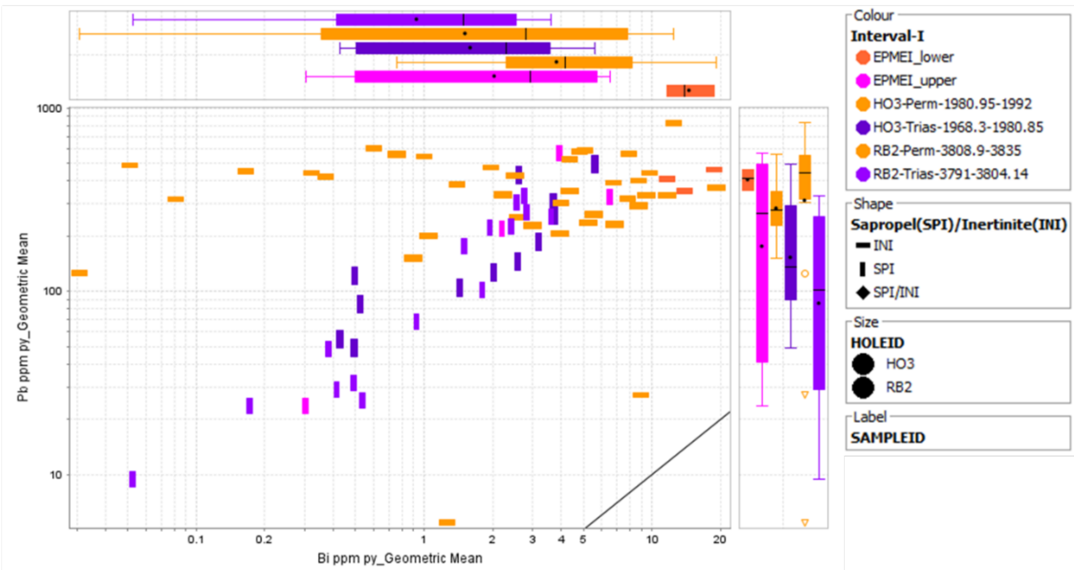

- Spearman correlation factor: Triassic 0.93, Permian 0.33

The scatter plots for other elements evidence a positive correlation could be observed for Ag, Pb, and Bi *vs* Cu; and Tl, Mo and Sb vs. Ni but only in Triassic pyrites.

Ag, Pb, Bi vs. Cu

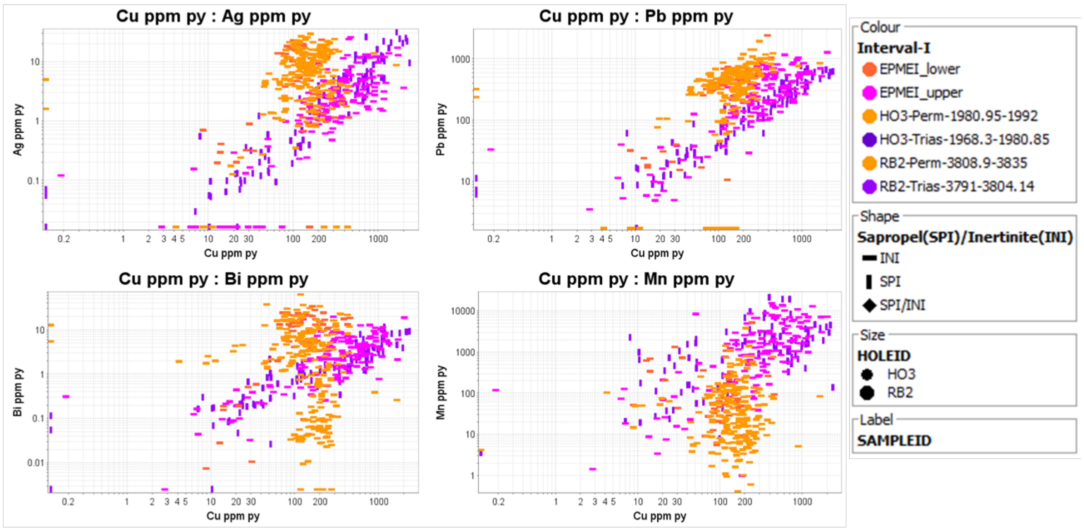

- Note correlation in Triassic samples, where variation of the element concentration spans orders of magnitude, and a weak correlation between Mn and Cu despite both are of high concentration in the Triassic pyrites

Selenium weakly and positively (Spearman correlation factor +0.55) correlates with Co and it is more obvious in nodules and in anomalous aggregates. The Se/Co ratio is at least treble in the Triassic, mainly due to high Co content in the Permian mudstones.

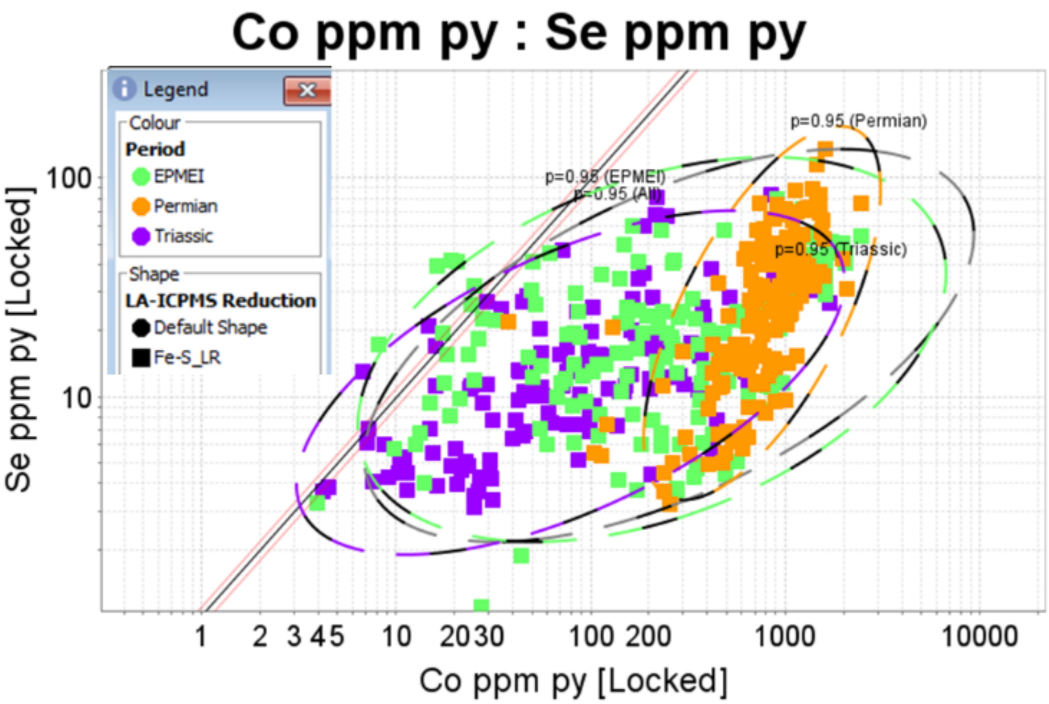

PCA

Principal Components Analysis confirmed that Zn and Cd always move together, Mo and Mn stay apart from other elements, whereas As and Cu have opposite engine vectors.

PCA Report: Transform None, Scaling true (288 rows) using correlation matrix

Summary	Count
Rows	288
Columns	15

Correlation	**Mn ppm py**	**Co ppm py**	**Ni ppm py**	**Cu ppm py**	**Zn ppm py**	**As ppm py**	**Se ppm py**	**Mo ppm py**	**Ag ppm py**	**Cd ppm py**	**Sb ppm py**	**Te ppm py**	**Tl ppm py**	**Pb ppm py**	**Bi ppm py**
Mn ppm p	1	-0.2986	-0.2555	0.402	0.2711	-0.1912	0.1332	0.0637	0.1958	0.1304	0.2998	0.4121	-0.2246	0.1006	0.01759
Co ppm p	-0.2986	1	0.5782	-0.1956	-0.09312	0.4683	0.1653	0.1512	0.126	-0.0203	0.2212	0.0977	0.4587	0.5232	0.3826
Ni ppm py	-0.2555	0.5782	1	-0.2082	-0.1398	0.7036	0.05575	0.4013	0.2196	-0.09973	0.3635	-0.1309	0.7371	0.3208	-0.09789
Cu ppm p	0.402	-0.1956	-0.2082	1	0.3454	-0.1962	0.2621	0.03246	0.3545	0.1855	0.2385	0.2343	-0.1821	0.3886	0.2252
Zn ppm p	0.2711	-0.09312	-0.1398	0.3454	1	-0.06505	0.2763	0.03979	0.2878	0.504	0.2554	0.2348	-0.117	0.0542	0.02411
As ppm py	-0.1912	0.4683	0.7036	-0.1962	-0.06505	1	0.04446	0.1346	0.2462	-0.04228	0.259	0.04498	0.5557	0.03544	0.08183
Se ppm py	0.1332	0.1653	0.05575	0.2621	0.2763	0.04446	1	0.2917	0.3712	0.1507	0.4459	0.3655	0.03221	0.3707	0.1648
Mo ppm p	0.0637	0.1512	0.4013	0.03246	0.03979	0.1346	0.2917	1	0.1828	0.1787	0.4259	0.02095	0.4826	0.2783	-0.1498
Ag ppm p	0.1958	0.126	0.2196	0.3545	0.2878	0.2462	0.3712	0.1828	1	0.1015	0.4306	0.2245	0.2401	0.2228	0.03398
Cd ppm p	0.1304	-0.0203	-0.09973	0.1855	0.504	-0.04228	0.1507	0.1787	0.1015	1	0.2924	0.05344	-0.03848	0.02981	0.00986
Sb ppm py	0.2998	0.2212	0.3635	0.2385	0.2554	0.259	0.4459	0.4259	0.4306	0.2924	1	0.4898	0.2026	0.384	0.09463
Te ppm py	0.4121	0.0977	-0.1309	0.2343	0.2348	0.04498	0.3655	0.02095	0.2245	0.05344	0.4898	1	-0.1156	0.2342	0.4333
Tl ppm py	-0.2246	0.4587	0.7371	-0.1821	-0.117	0.5557	0.03221	0.4826	0.2401	-0.03848	0.2026	-0.1156	1	0.1735	-0.06543
Pb ppm p	0.1006	0.5232	0.3208	0.3886	0.0542	0.03544	0.3707	0.2783	0.2228	0.02981	0.384	0.2342	0.1735	1	0.4022
Bi ppm py	0.01759	0.3826	-0.09789	0.2252	0.02411	0.08183	0.1648	-0.1498	0.03398	0.00986	0.09463	0.4333	-0.06543	0.4022	1

	Mn ppm py	**Co ppm py**	**Ni ppm py**	**Cu ppm py**	**Zn ppm py**	**As ppm py**	**Se ppm py**	**Mo ppm py**	**Ag ppm py**	**Cd ppm py**	**Sb ppm py**	**Te ppm py**	**Tl ppm py**	**Pb ppm py**	**Bi ppm py**
Eigenvect	PC1	PC2	PC3	PC4	PC5	PC6	PC7	PC8	PC9	PC10	PC11	PC12	PC13	PC14	PC15
Mn ppm p	0.04568	0.3694	0.1098	0.3611	0.2013	0.1117	0.4557	0.1547	0.2905	0.06618	0.5679	0.06556	0.1092	0.06605	0.05091
Co ppm p	0.3246	-0.23	-0.3327	-0.2537	-0.08171	0.03232	0.01214	0.2422	0.166	0.2985	0.1535	-0.01798	-0.2534	0.6288	0.00469
Ni ppm py	0.3491	-0.3501	0.1021	0.05321	0.03623	-0.07654	0.1347	0.2576	0.01602	-0.1765	-0.09106	0.01753	0.1289	-0.1773	0.7501
Cu ppm p	0.1144	0.3788	-0.02682	0.1297	-0.2148	-0.5122	0.2264	-0.1528	-0.1874	-0.4098	-0.1494	-0.1919	-0.1733	0.3749	0.1003
Zn ppm p	0.1126	0.3197	0.2527	-0.4701	0.09772	-0.1456	-0.02559	0.1099	0.6197	-0.09192	-0.3267	0.2073	0.1064	-0.00977	-0.05697
As ppm py	0.2857	-0.2809	0.01932	-0.1164	0.4802	-0.1176	0.08765	-0.0316	-0.112	-0.4672	0.2136	0.2283	-0.3121	-0.1254	-0.3615
Se ppm py	0.2782	0.2174	-0.00987	0.04274	-0.1304	0.1183	-0.7286	0.00814	0.08314	-0.3266	0.3952	-0.1419	0.1267	0.0189	0.072
Mo ppm p	0.2847	-0.05195	0.3356	0.2156	-0.3959	0.3428	0.04244	-0.4235	0.0884	0.02321	-0.08752	0.4353	-0.301	0.06977	0.02519
Ag ppm p	0.2921	0.1413	0.1629	0.1285	0.2402	-0.53	-0.2639	-0.1283	-0.1601	0.5916	0.05849	0.1486	-0.07953	-0.1292	0.05387
Cd ppm p	0.1007	0.2105	0.3095	-0.6359	-0.1351	0.1702	0.2126	-0.05979	-0.3739	0.1093	0.2964	-0.2365	-0.1219	-0.1576	0.1195
Sb ppm py	0.3823	0.1673	0.1354	0.09664	0.1296	0.2795	0.03709	0.2867	-0.4361	0.0124	-0.3158	0.09972	0.4448	0.2362	-0.2571
Te ppm py	0.1984	0.3014	-0.2561	0.1129	0.4066	0.3828	-0.02094	-0.1326	0.08575	0.06271	-0.33	-0.3633	-0.4037	-0.1436	0.1607
Tl ppm py	0.3065	-0.3248	0.1692	0.05033	-0.0063	-0.07292	0.1528	-0.4105	0.266	0.06891	0.00501	-0.567	0.3384	0.00875	-0.2461
Pb ppm p	0.3306	0.0905	-0.3081	0.08799	-0.482	-0.1083	0.1502	0.3389	0.06979	0.05008	-0.02953	-0.0422	-0.1055	-0.5319	-0.307
Bi ppm py	0.1437	0.1297	-0.5994	-0.2226	0.03212	0.01564	0.1386	-0.4817	-0.05449	-0.01375	0.07884	0.3321	0.3926	-0.07915	0.1452

	Eigenvalu	Percent	Cumulative %
PC1	3.728	24.85	24.85
PC2	3.139	20.93	45.78
PC3	1.684	11.23	57.01
PC4	1.11	7.403	64.41
PC5	1.05	7.002	71.41
PC6	0.9137	6.091	77.51
PC7	0.7733	5.156	82.66
PC8	0.5256	3.504	86.16
PC9	0.4767	3.178	89.34
PC10	0.4351	2.901	92.24
PC11	0.3867	2.578	94.82
PC12	0.2752	1.834	96.66
PC13	0.2233	1.488	98.14
PC14	0.1744	1.163	99.31
PC15	0.1039	0.6926	100

Scaled Co	PC1	PC2	PC3	PC4	PC5	PC6	PC7	PC8	PC9	PC10	PC11	PC12	PC13	PC14	PC15
Mn ppm p	0.09	0.65	0.14	0.38	0.21	0.11	0.40	0.11	0.20	0.04	0.35	0.03	0.05	0.03	0.02
Co ppm p	0.63	-0.41	-0.43	-0.27	-0.08	0.03	0.01	0.18	0.11	0.20	0.10	-0.01	-0.12	0.26	0.00
Ni ppm py	0.67	-0.62	0.13	0.06	0.04	-0.07	0.12	0.19	0.01	-0.12	-0.06	0.01	0.06	-0.07	0.24
Cu ppm p	0.22	0.67	-0.03	0.14	-0.22	-0.49	0.20	-0.11	-0.13	-0.27	-0.09	-0.10	-0.08	0.16	0.03
Zn ppm p	0.22	0.57	0.33	-0.50	0.10	-0.14	-0.02	0.08	0.43	-0.06	-0.20	0.11	0.05	0.00	-0.02
As ppm py	0.55	-0.50	0.03	-0.12	0.49	-0.11	0.08	-0.02	-0.08	-0.31	0.13	0.12	-0.15	-0.05	-0.12
Se ppm py	0.54	0.39	-0.01	0.05	-0.13	0.11	-0.64	0.01	0.06	-0.22	0.25	-0.07	0.06	0.01	0.02
Mo ppm p	0.55	-0.09	0.44	0.23	-0.41	0.33	0.04	-0.31	0.06	0.02	-0.05	0.23	-0.14	0.03	0.01
Ag ppm p	0.56	0.25	0.21	0.14	0.25	-0.51	-0.23	-0.09	-0.11	0.39	0.04	0.08	-0.04	-0.05	0.02
Cd ppm p	0.19	0.37	0.40	-0.67	-0.14	0.16	0.19	-0.04	-0.26	0.07	0.18	-0.12	-0.06	-0.07	0.04
Sb ppm py	0.74	0.30	0.18	0.10	0.13	0.27	0.03	0.21	-0.30	0.01	-0.20	0.05	0.21	0.10	-0.08
Te ppm py	0.38	0.53	-0.33	0.12	0.42	0.37	-0.02	-0.10	0.06	0.04	-0.21	-0.19	-0.19	-0.06	0.05
Tl ppm py	0.59	-0.58	0.22	0.05	-0.01	-0.07	0.13	-0.30	0.18	0.05	0.00	-0.30	0.16	0.00	-0.08
Pb ppm p	0.64	0.16	-0.40	0.09	-0.49	-0.10	0.13	0.25	0.05	0.03	-0.02	-0.02	-0.05	-0.22	-0.10
Bi ppm py	0.28	0.23	-0.78	-0.23	0.03	0.01	0.12	-0.35	-0.04	-0.01	0.05	0.17	0.19	-0.03	0.05

Pb and Se-rich deteriorated (sooty) aggregates

Degraded oxidised framboidal pyrite aggregate Redback-2_3808.13. Barite globules and scarce pyrite framboids in a smectite–chlorite clayish matrix from the same sample.

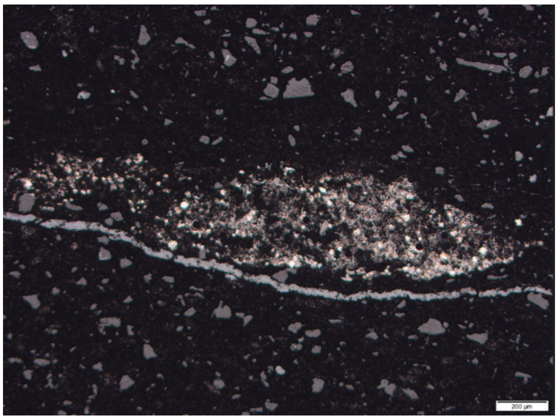

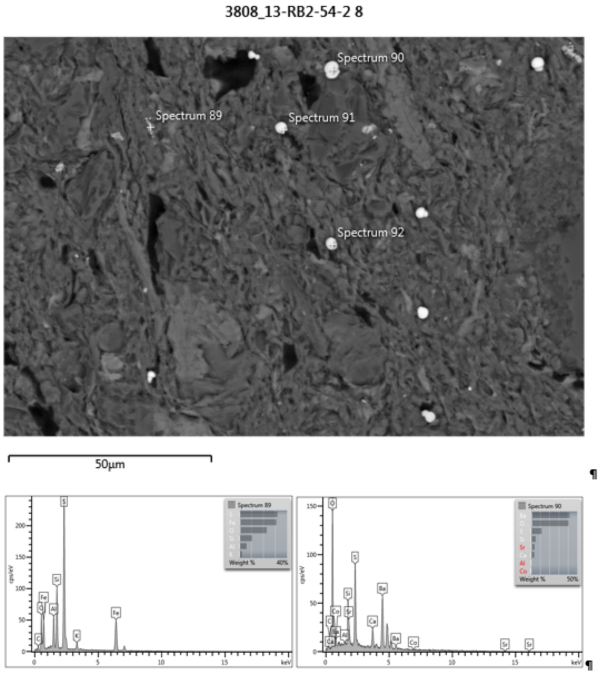

The distribution of the trace elements in pyrite from this horizon RB2-3809.73 is bimodal and reveals anomalously high Pb (6000–24 000 ppm) and Se (500–2000 ppm) in pyrite likely corresponding to the deteriorated aggregates.

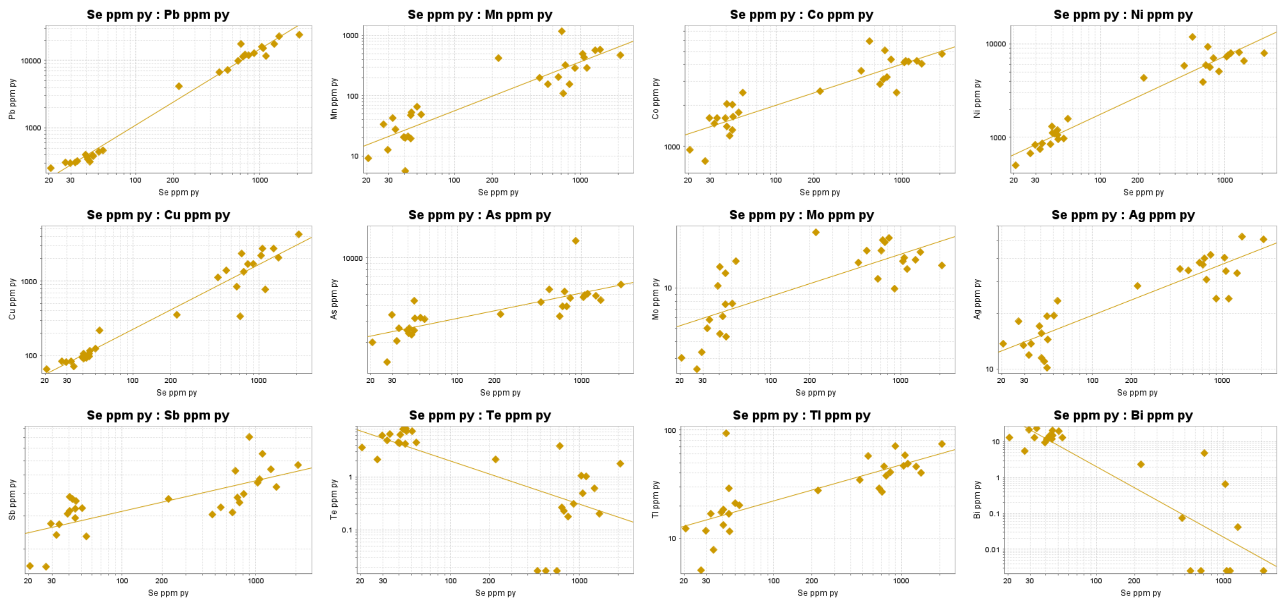

HO3-1987.03 fossils (polished mount 2500 mm in diameter). Reflected and UV light.

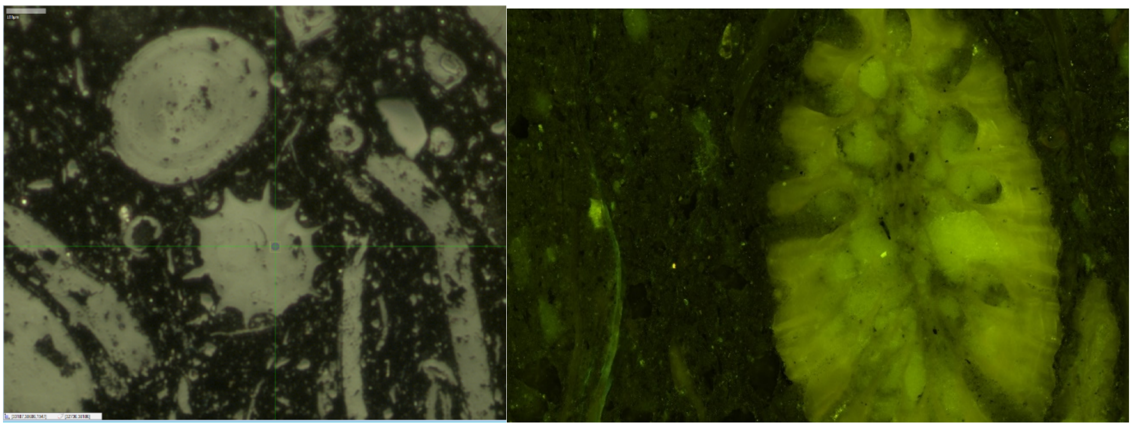

References

Belousov, I., Danyushevsky, L., Olin P., Gilbert, S., & Thompson, J. (2014). New calibration standard for LA-ICPMS analysis of sulphides. AGU, 2014 Fall Meeting. Retrieved from https://agu.confex.com/agu/fm14/webprogram/Paper19453.html.

Danyushevsky, L., Robinson, P., Gilbert, S., Norman, M., Large, R., McGoldrick, P., & Shelley, M. (2011). Routine quantitative multi-element analysis of sulphide minerals by laser ablation ICP-MS: Standard development and consideration of matrix effects. Geochemistry: Exploration, Environment, Analysis, 11(1), 51–60. https://doi.org/10.1144/1467-7873/09-244

Georgiev, S. V., Stein, H. J., Yang, G., Hannah, J. L., Böttcher, M. E., Grice, K., Holman, A. I., Turgeon, S., Simonsen, S., & Cloquet, C. (2020). Late Permian–Early Triassic environmental changes recorded by multi-isotope (Re–Os–N–Hg) data and trace metal distribution from the Hovea-3 section, Western Australia. Gondwana Research, 88, 353–372. https://doi.org/10.1016/j.gr.2020.07.007

Gilbert, S. E., Danyushevsky, L. V., Rodemann, T., Shimizu, N., Gurenko, A., Meffre, S., Thomas, H., Large, R. R., & Death, D. (2014). Optimisation of laser parameters for the analysis of sulphur isotopes in sulphide minerals by laser ablation ICP-MS. Journal of Analytical Atomic Spectrometry, 29(6), 1042. https://doi.org/10.1039/c4ja00011k

Gregory, D. D., Large, R. R., Halpin, J. A., Lounejeva, E., Lyons, T. W., Wu, S., Danyushevsky, L., Sack, P. J., Chappaz, A., Maslennikov, V. V., & Bull, S. W. (2015). Trace element content of sedimentary pyrite in black shales. Economic Geology, 110(6), 1389–1410. https://doi.org/10.2113/econgeo.110.6.1389

Jochum, K. P. (2014). Reference Materials in Geochemical and Environmental Research. Analytical Geochemistry/Inorganic Instrumental Analysis (2nd ed., Vol. 15). Elsevier Ltd. https://doi.org/10.1016/B978-0-08-095975-7.01403-0

Large, R., Halpin, J., Danyushevsky, L., Maslennikov, V., Bull, S., Long, J., Gregory, D., Lounejeva, E., Lyons, T., Sack, P., McGoldrick, P., & Calver, C. (2014). Trace element content of sedimentary pyrite as a new proxy for deep-time ocean–atmosphere evolution. Earth and Planetary Science Letters, 389, 209–220. https://doi.org/10.1016/j.epsl.2013.12.020

Lounejeva, E., Steadman, J. A., Rodemann, T., Large, R. R., Danyushevsky, L., Mantle, D., Grice, K., & Algeo, T. J. (2021). Marcasite at the Permian–Triassic Transition. In R. E. Ernst, A. J. Dickson & A. Bekker (Eds.), Large Igneous Provinces https://doi.org/10.1002/9781119507444.ch16

Purcell R. (2010). Redback-2 Completion report. Origin Ltd.

Sial, A., Chen, J., Lacerda, L., Korte, C., Spangenberg, J., Silva-Tamayo, J., Gaucher, C., Ferreira, V., Barbosa, J., Pereira, N., & Benigno, A. (2020). Globally enhanced Hg deposition and Hg isotopes in sections straddling the Permian–Triassic boundary: Link to volcanism. Palaeogeography, Palaeoclimatology, Palaeoecology, 540, 109537. https://doi.org/10.1016/j.palaeo.2019.109537

Stepanov, A., Danyushevsky, L., Large, R., Mukherjee, I., & Zhukova, I. (2020). Deconvolution of the composition of fine-grained pyrite in sedimentary matrix by regression of time-resolved LA-ICP-MS data. American Mineralogist, 105(6), 820–832. https://doi.org/10.2138/am-2020-7202

Thomas, B. M., Willink, R. J., Grice, K., Twitchett, R. J., Purcell, R. R., Archbold, N. W., George, A. D., Tye, S., Alexander, R., Foster, C. B., & Barber, C. J. (2004). Unique marine Permian–Triassic boundary section from Western Australia. Australian Journal of Earth Sciences, 51(3), 423–430. https://doi.org/10.1111/j.1400-0952.2004.01066.x

Lounejeva et al. (2023). Supplemental data
Australian Journal of Earth Sciences, 70(5), https://doi.org/10.1080/08120099.2023.2200476

Petrographic observations

This document contains some petrographic observations about pyrite and other textures in Redback-2 core sample. Here we preserve double sample ID, the depth and the number given during sampling.

3788.7_RB2-06A	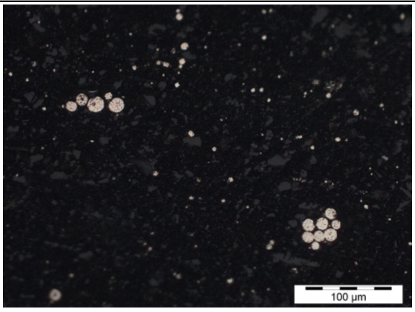	Framboidal pyrite
3790.0_RB2-09 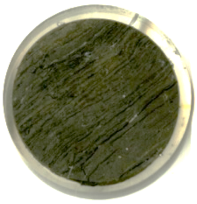	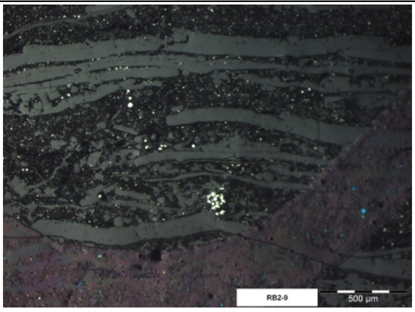	Framboidal pyrite in a microlaminated mudstone
3791.7_RB2-10 	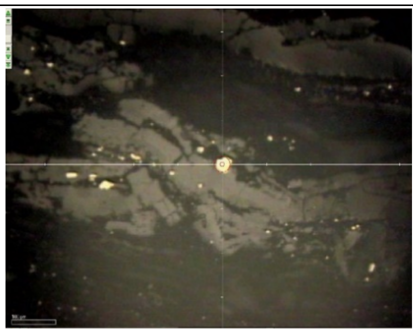	Disseminated pyrite in a brittle microlaminated siltstone
3792.9_RB2-11	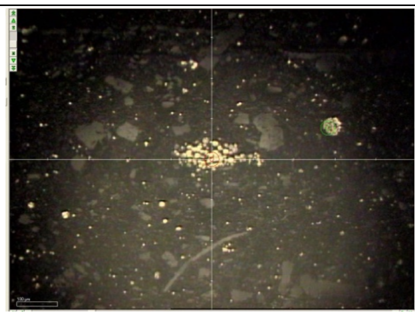	Framboidal aggregate ~100 um
3793.8_RB2-12 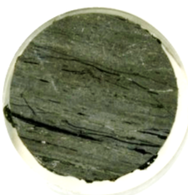	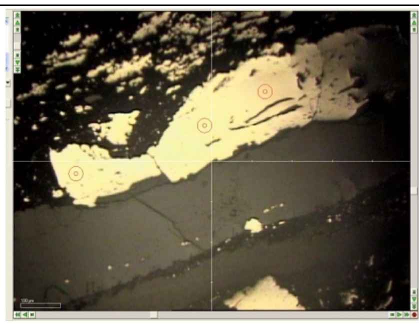	Only diagenetic

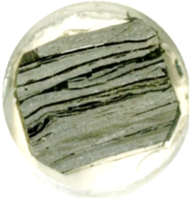		
3795.7_RB2-13 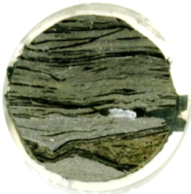	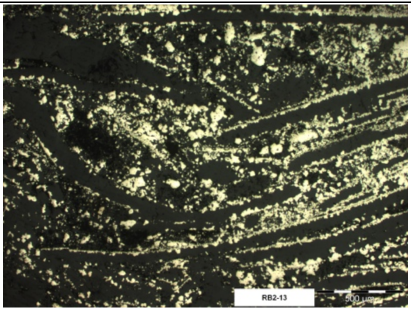	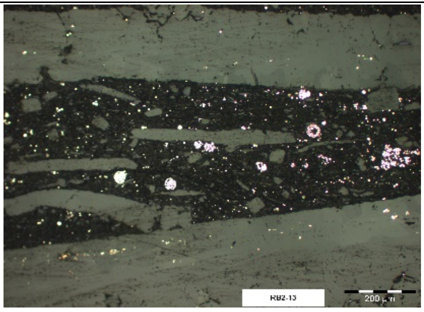
3796.8_RB2-14 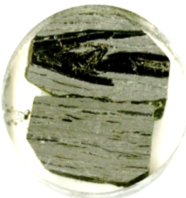	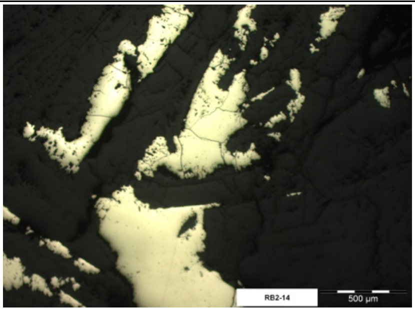	Only diagenetic anhedral pyrite.
3797.3_RB2-5B	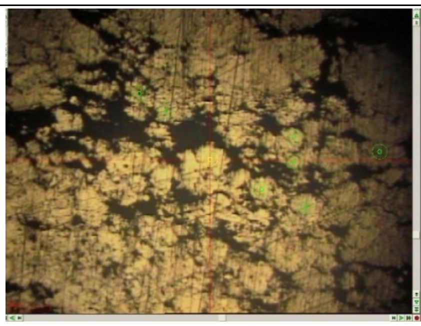	Porous pyrite nodule Molybdenum ~ 500 ppm
3797.8_RB2-15 	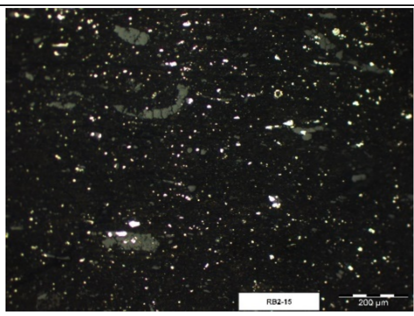	Image and 3 analyses
3798.3_RB2-16 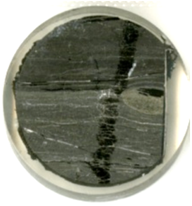	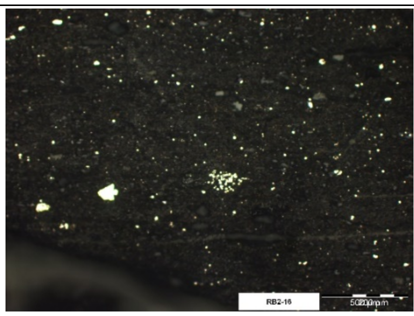	Framboids and a massive pyrite nodule

	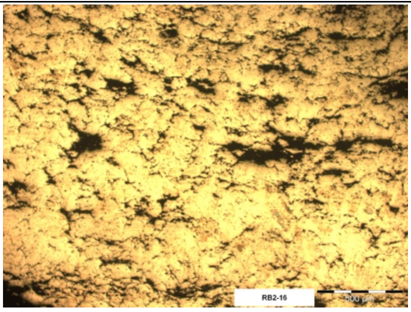	
3799.2_RB2-18 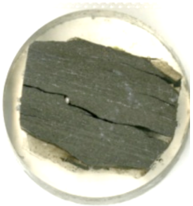		Framboidal, sooty
3799.93_RB2-19 	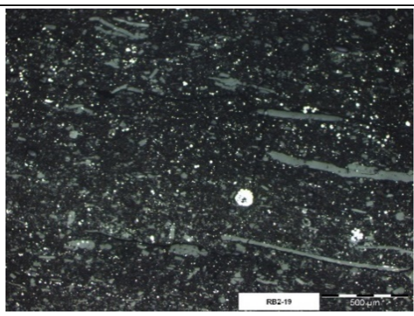	Framboidal
3800.4_RB2-20 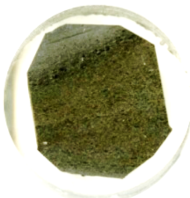	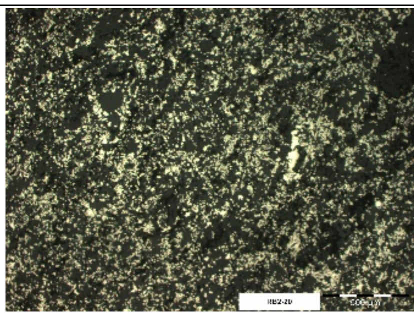	Porous pyrite nodule, the entire sample
3801.12_RB2-21 	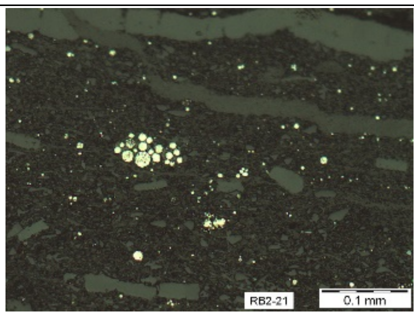	Framboidal pyrite
3801.7_RB2-22 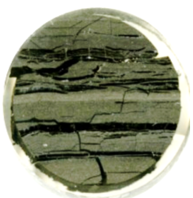	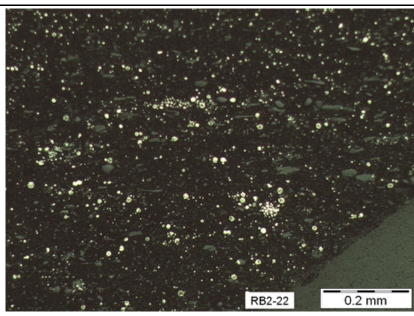	Framboidal pyrite

3802.1_RB2-23 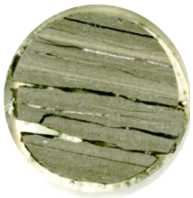	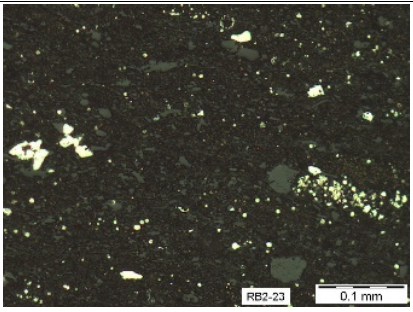	Framboidal pyrite and disseminated
3803.2_RB2-24A 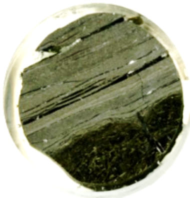	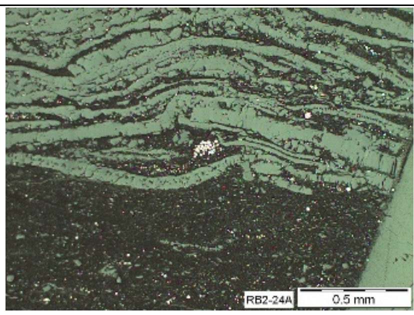	Boundary between microlaminated and organic-rich black shale with framboidal aggregates
3804.6_RB2-25 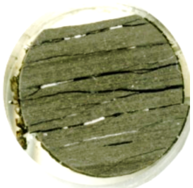	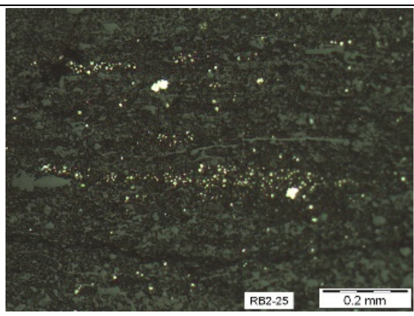	Framboidal pyrite and disseminated
3805.4_RB2-26 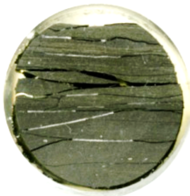	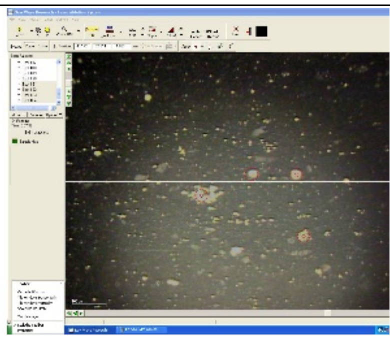	Framboidal pyrite and disseminated
3806.1_RB-51 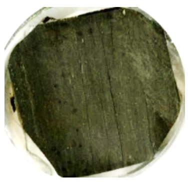	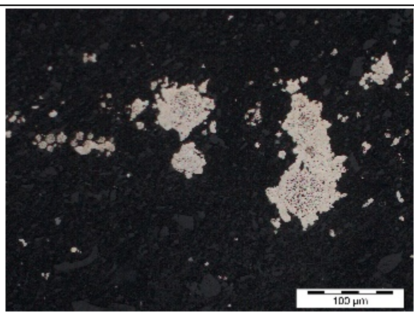	Framboidal pyrite aggregates, spongy aggregates and disseminated

3806.51_RB2-56 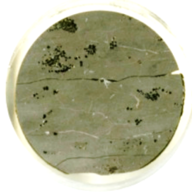 and 3806.55_RB2-27	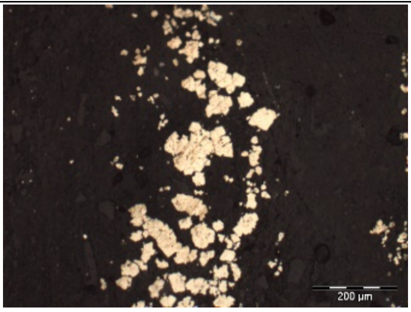 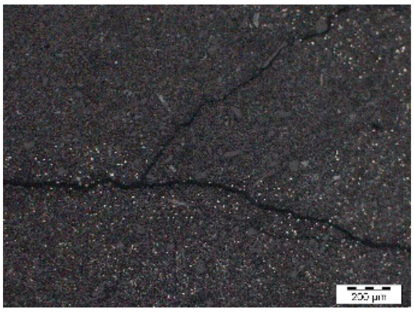	Euhedral pyrite and marcasite, and very fine disseminated pyrite
3807.1_RB2-52 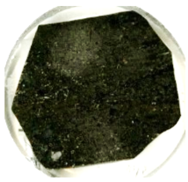	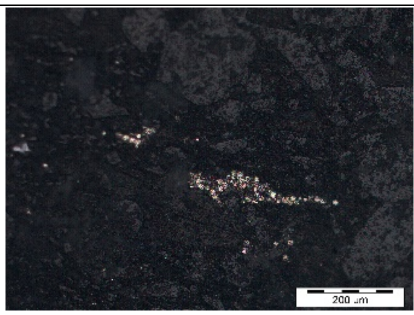	Angular siderite and very fine framboids
3807.35_RB2-53	 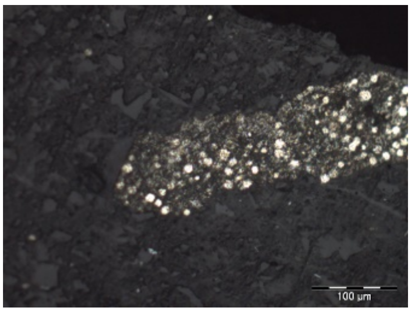	Degraded framboidal pyrite aggregates

3808.13_RB2-54 	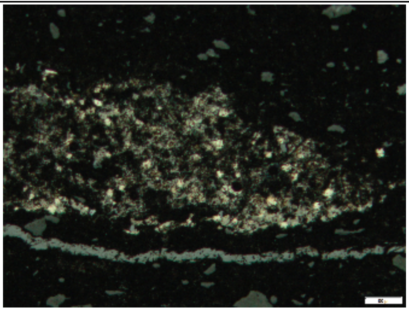	Degraded oxidised framboidal pyrite aggregate. Anomalously high Pb (6000–24 000 ppm) and Se (500–2000 ppm)
3808.9_RB2-28 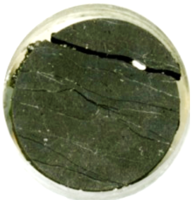	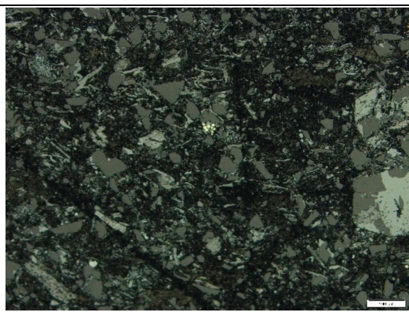	Rare framboids in a poorly sorted clastic matrix
3809.6_RB2-29 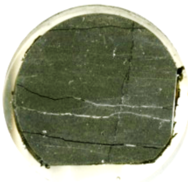	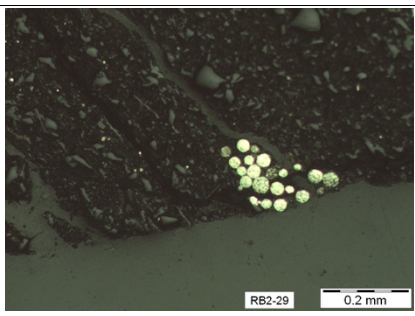	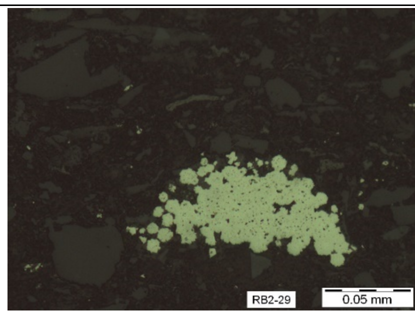 Spongy framboidal aggregate
3809.73_RB2-55	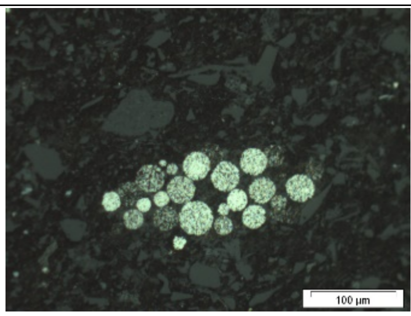 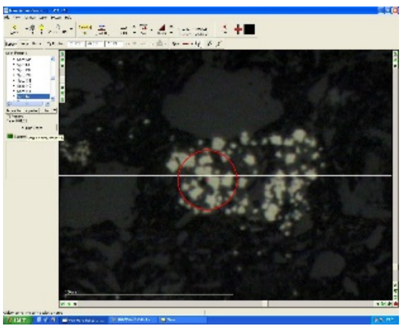	Framboids 35 um each Highly oxidised framboidal aggreagte (molty)

3810.4_RB2-45	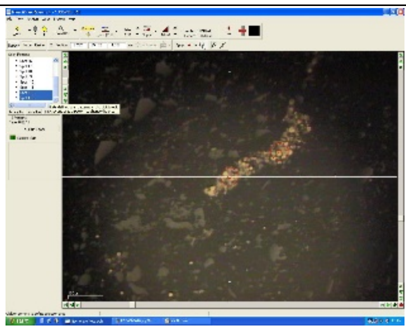	Framboidal aggregates and single framboids
3811.0_RB2-46	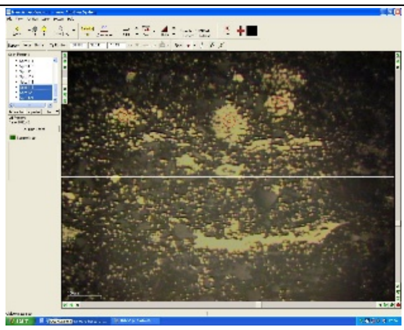	Single and framboidal aggregates
3811.8_RB2-30 	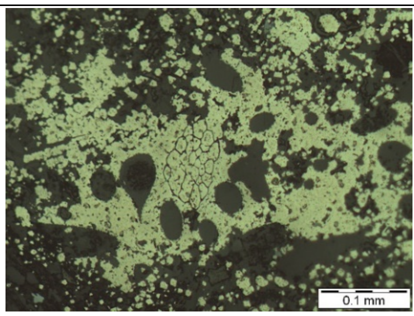	An example of framboidal nodule growing. Some boundaries between individual framboids still remain in this pyrite nodule, likely of diagenetic origin.
3812.2_RB2-47	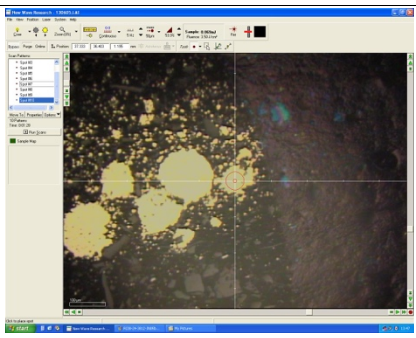	Framboidal and nodule
3812.7_RB2-31 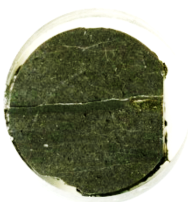	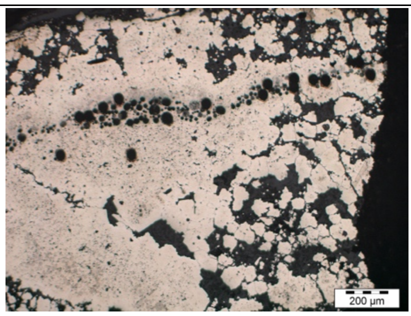	Pyrite nodule, likely diagenetic. 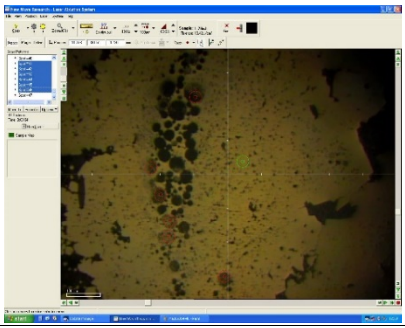

3813.6_RB2-48	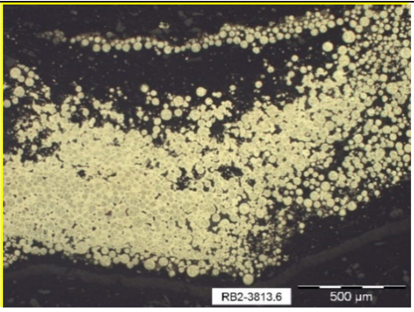	Pyrite nodule with well-preserved framboidal texture.
3814.5-RB2-2	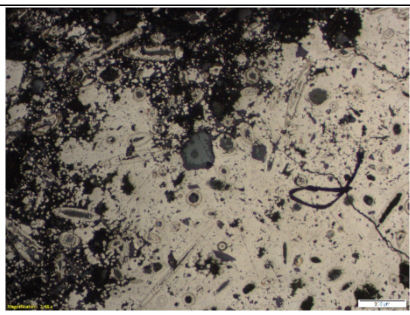	Pyritised fossil nodule. High As–Ni–Co, comparable with RB2-3812.7 Also, see the LA-ICPMS image in archives. 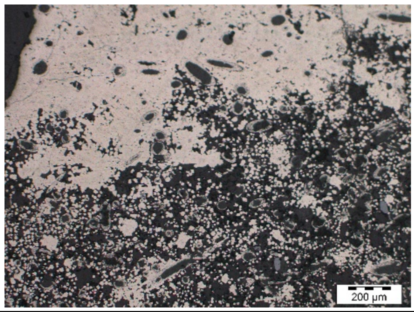
3815.95_RB2-49	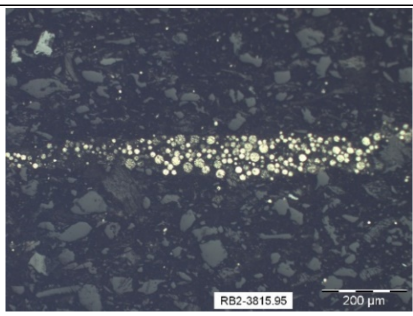	Framboidal pyrite aggregate
3816.9_RB2-32 	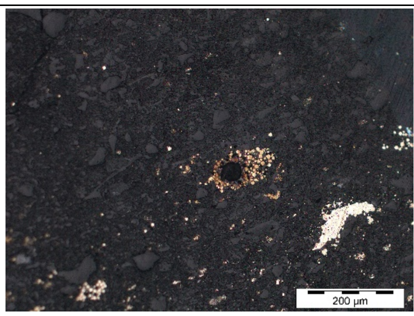	Framboidal pyrite aggregates
3818.1_RB2-33 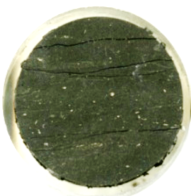	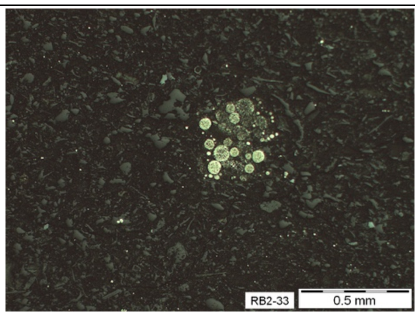	Framboidal pyrite aggregates and single framboids in the matrix

3821.3_RB2-34 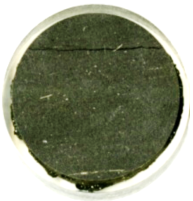	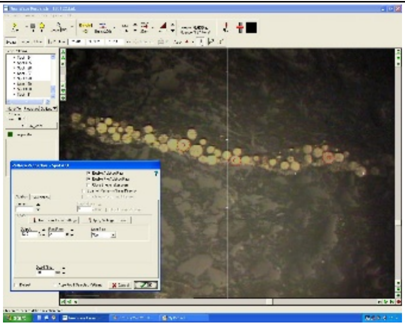	Framboidal pyrite aggregate
3823.8_RB2-35 	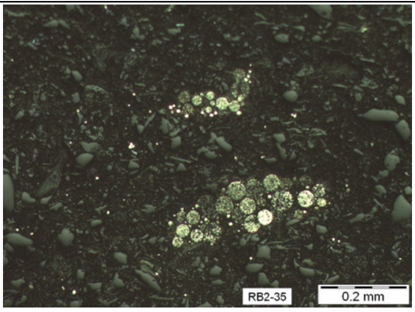	Nodule (used by D Gregory for S isotopes) and framboidal pyrite
3825.6_RB2-36 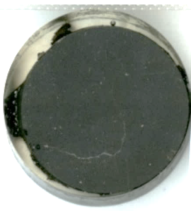	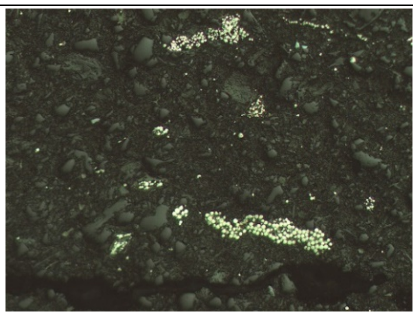	
3827.4_RB2-37 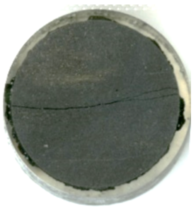	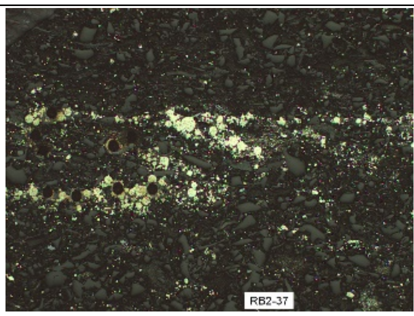	
3830.6_RB2-38 	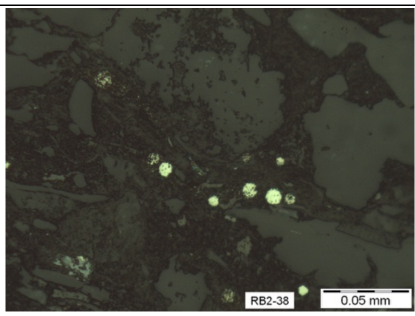	

3831.2_RB2-39 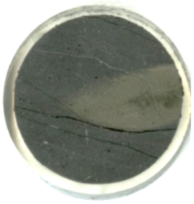	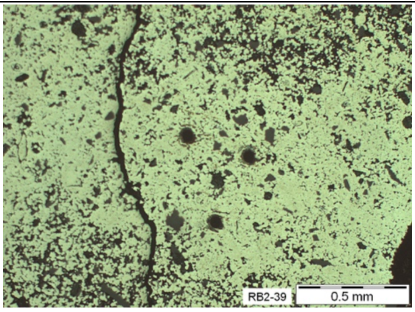	Pyrite nodule ~2 cm large and framboidal aggregates
3832.1_RB2-01	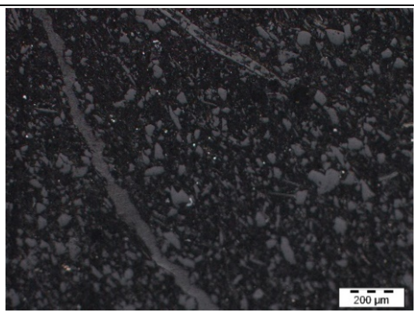	Scarce framboidal pyrite
3834.3_RB2-40 	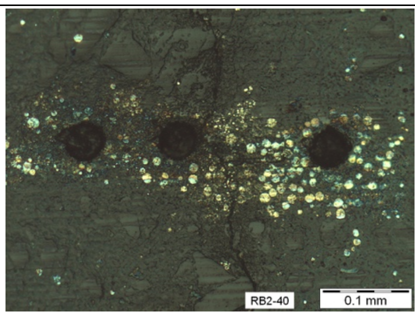	Framboidal aggregate
3835.3_RB2-50	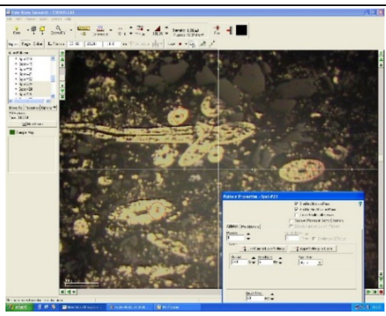	Pyritised fossils, likely sponge spicules